WILEY-VCH

# Ultrasensitive Molecular Detection by Imaging of Centimeter-scale Metasurfaces with a Deterministic Gradient Geometry

*Siyi Min, Shijie Li, Zhouyang Zhu, Yu Liu, Chuwei Liang, Jingxuan Cai, Fei Han, Yuyan Li, Wenshan Cai, Xing Cheng*, and Wen-Di Li**

Dr. S. Min, Dr. S. Li, Dr. Z. Zhu, Y. Liu, C. Liang, Dr. J. Cai, Dr. W.-D. Li
Department of Mechanical Engineering
The University of Hong Kong
Pokfulam, Hong Kong 999077, China
E-mail: liwd@hku.hk
Dr. S. Min, Y. Liu, F. Han, Y. Li, Prof. X. Cheng
Southern University of Science and Technology
Shenzhen, Guangdong 518052, China
E-mail: chengx@sustech.edu.cn
Prof. W. Cai
School of Electrical and Computer Engineering
Georgia Institute of Technology
Atlanta 30332, USA

Keywords: molecular detection, image-based sensing scheme, centimeter-scale metasurfaces, deterministic gradient geometry

Highly sensitive detection of trace amounts of substances is crucial for broad applications in healthcare, environmental monitoring, antiterrorism, etc., where cost effectiveness and portability are often demanded. Here, we report an ultrasensitive sensor that can detect an angstrom-thick layer of adsorbed molecules through image acquisition and processing. The sensor features a centimeter-scale plasmonic metasurface with spatially varying geometry, where the light scattering is dependent on both the adsorbed substances and spatial locations. When illuminated with narrowband light (such as from an LED), the intensity pattern recorded on the metasurface changes with the surface-adsorbed molecules, enabling label-free, sensitive, and spectrometer-free molecular detection. The centimeter-scale size of the sensing area interfaces well with consumer-level imaging sensors on mobile devices without the need for microscopic optics and offers a high signal-to-noise ratio by leveraging the multimillion pixels for noise reduction. We experimentally demonstrate that a single layer of $Al_2O_3$ molecules deposited on the sensor, with a thickness of approximately one angstrom, can be detected by analyzing the images taken of the sensing chip. Furthermore, by integrating our sensor into a

microfluidic setup, we demonstrate quantitative detection of BSA/anti-BSA immune complex formation events, which agrees well with the Langmuir isotherm model.

Metasurfaces with metallic[1] and dielectric[2] nanophotonic building blocks manipulate light scattering in the subwavelength regime and are promising in broad applications.[3] The wavelength-dependent light scattering behavior at metasurface building blocks is highly sensitive to the structure's geometric shape and size as well as to the local environment in the vicinity of the structure. The strong dependency of the light scattering spectrum on the local environment near nanostructures can be used for highly sensitive refractometric sensing of substances adsorbed or attached to nanostructures.[4] Specifically, with the subwavelength size of metasurface building blocks and highly concentrated electrical field near the surface of metasurfaces, various dielectric and plasmonic metasurface devices have been intensively investigated for the detection of hazardous gas,[5] water and air pollution,[6] biomarkers[7] and many other threat-[8] and disease-relevant[9] species. Spectroscopic characterization is typically required to detect spectral changes in the scattered light caused by the existence of a small amount of target substances. When the amount of a target substance is very small, high-sensitivity and high-spectral-resolution spectrometers are needed, which are expensive, bulky, and skill-demanding. This often hinders the daily applications of molecular detection for food safety, environmental quality monitoring, point-of-care biomedical detection, etc., which require cost effectiveness, compactness, and easy operation.

Space-multiplexed imaging-based molecule detection using spatially varying nanostructures has recently been developed to overcome the aforementioned difficulties[10-12]. Due to the structure-dependent light scattering property, properly designed spatially varying nanostructures have position-dependent reflectance or transmittance under narrowband light

illumination, therefore exhibiting an intensity pattern. Adsorption or attachment of analyte molecules on the metasurface alters the intensity pattern, which can be recorded by a camera and indicate the existence of analyte molecules. Both pixelated metasurfaces,[12] where the geometry of the nanostructure building blocks discretely vary, and gradient metasurfaces,[10] where the geometry continuously varies, have been demonstrated. By employing an advanced design of nanostructure building blocks with high sensing performance, this new sensing mechanism has shown an impressive capability of achieving high sensitivity using a greatly simplified setup. However, most works reported thus far have been realized by using electron-beam lithography, with a limited sensing area of a few hundred microns and typically containing ~$10^5$ or fewer unit cells. A microscopic setup is still often needed to couple the tiny sensing chip with the imaging sensor, and the limited number of metasurface unit cells results in a low signal-to-noise ratio in the intensity pattern.

Here, we report a centimeter-scale plasmonic metasurface with regular but spatially varying pillars and holes for ultrasensitive, label-free, and spectrometer-free detection of single-layer molecules adsorbed on the surface. The centimeter-scale size of the sensing area interfaces well with consumer-level imaging sensors on mobile devices without the need for microscopic optics and offers a high signal-to-noise ratio by leveraging the multimillion pixels for noise reduction. This novel sensing scheme is expected to be a promising platform for point-of-care and lab-on-chip applications, which can be realized using off-the-shelf monochromatic light sources and commercial image sensors.

In the new sensing scheme, continuously varying gradient plasmonic metasurfaces are applied to map spectral information to spatial locations, enabling space-multiplexed imaging-based quantitative analyte detection. Specifically, the sensing chip is illuminated by a narrowband light source, and the transmission pattern is recorded by a commercial image sensor (**Figure**

**1**a). The local refractive index change induced by the adsorption or attachment of analyte molecules on the sensing chip alters the intensity pattern recorded by a camera, indicating the existence of analyte molecules (Figure 1a). An image processing algorithm is developed to calculate the intensity distribution and retrieve the pattern variation to quantitatively detect the analyte substances.

Our nanophotonic sensing chip is designed to consist a metasurface with concentric gradient nanostructures. Along the radial direction, due to the structure-dependent light scattering property, the continuously varying nanostructures have different transmission spectra (Figure 1b). Therefore, under narrowband light illumination, the metasurface exhibits a concentric intensity pattern, which can be expressed as a curve of transmission intensity versus position from the center to the edge (Figure 1d). Since the wavelength-dependent light scattering behavior at metasurface building blocks is highly sensitive to the local environment in the vicinity of the structure (Figure 1b), the intensity value at each position also changes with the local refractive index (Figure 1d). Taking two different positions as examples, the zoomed-in transmission spectra in the resonance regions of positions A and B are shown in Figure 1c, where the illuminating narrowband light source is marked as the red strip. For position A, the resonance wavelength under $n_1$ is shorter than the wavelength of the illumination light source; in contrast, the resonance at position B occurs at a wavelength longer than that of the light source. With the refractive index increasing from $n_1$ to $n_3$, the resonance peaks are both shifted to longer wavelengths, which leads to an intensity decrease at position A and an intensity increase at position B (Figure 1e). The intensity changes at each position constitute the changes in the intensity-position curve. By retrieving the changes in intensity-position curves, such as those in the dip position, the analyte-induced refractive index change can be quantitatively analyzed.

The metasurface in our work is fabricated using a homemade interference lithography setup.[13] Conventional interference lithography emphasizes pattern uniformity; therefore, a long beam expansion distance to achieve a uniform exposure intensity over the patterning area is desired. To fabricate spatially varying structures, the expansion distance is intentionally set short so that we can utilize the non-uniform Gaussian-shaped intensity distribution of the two coherent beams to realize spatially varying patterns with circular symmetry. Figure S1, Supporting Information, shows the intensity distributions at various expansion distances. To generate a metasurface with a diameter of approximately 2 cm in this work, the beam expansion distance is set to 25 cm. **Figure 2**a schematically shows that two orthogonal interference lithography exposures using Gaussian-shaped beams result in a two-dimensional periodic pattern with a gradient profile from the center to the edge. The red lines in the zoomed-in region represent the threshold exposure intensity for clearing the photoresist, therefore they also represent the outlines of the photoresist patterns. The exposure patterns on the positive-tone photoresist show pillars at the center, where the Gaussian beam has the maximum intensity. The diameter of the pillars increases with increasing distance from the center. Nearby pillars start to merge, and the overall pattern evolves into a hole array with the diameter of the holes decreasing as the distance from the center further increases. The metasurface period is chosen to be 550 nm so that the fabricated plasmonic nanostructures exhibit resonance behaviors at approximately 800 nm wavelength, which is within the working spectral range of cost-effective commerical image sensor modules.

The sensing chip is designed to contain gold nanopillars and nanoholes. These well-studied plasmonic structures can be fabricated through robust process and modeled by numerical simulation with good accuracy. A sensing chip of a gold metasurface (Figure 2b) on a glass substrate was fabricated using thermal nanoimprint lithography[14] with a silicon mold with a concentric gradient pattern replicated from the photoresist pattern. The detailed fabrication flow diagram and scanning electron microscopy (SEM) images of the key fabrication steps are

shown in Figure S2 and Figure S3, Supporting Information, respectively. The nanostructure filling ratio increases from 5.6% to 72.9% from the center to the edge along the radial direction, as shown in Figure 2c, where the insets are SEM images of unit structures on the metasurface at the data point positions, with the error bars representing the calculated standard deviation. The SEM sweeping on the gradient gold metasurface sensing chip is shown in Figure S4, Supporting Information. It contains 10 × 10 images with x and y intervals of 1 mm from the center to the corner. The metasurface has a gradient profile on the millimeter scale but is relatively uniform on the micrometer scale (the standard deviation of the duty ratio is less than 0.0382). Specifically, the pillar diameter gradient is 25.5 nm $mm^{-1}$ at R = 4.2 mm position on the metasurface, which promises a high resolution for the sensing chip. The theoretical morphology characterization at the corresponding positions of the SEM images is shown in Figure S5, Supporting Information, which well matches the measured results.

The transmission spectra on the gradient plasmonic metasurface are experimentally characterized from 600 nm to 950 nm at positions along the radial direction from the center (R = 0 mm) to the edge (R = 9 mm) with a step of 1 mm, as plotted in **Figure** 3a. The transmission dip shifts from 790 nm to 910 nm as the pillar diameter gradually increases with the distance from the center. At R = 7 mm, the structure transits from nanopillars to nanosquares, and the resonance wavelength is further redshifted to longer than 950 nm. When the distance from the center increases beyond 8 mm, nearby pillars start to merge into holes, and then the diameter of the holes decreases. The resonance wavelengths of the holes correspondingly decrease. The variation in transmission spectra induced by the spatially varying geometric shape and size of the nanostructures results in the featured transmission intensity pattern of the gradient plasmonic metasurface under a monochromatic light source. Numerical modeling is also used to calculate the theoretical transmission spectra (Figure 3b). The simulated resonance wavelength shift is consistent with the experimental results. Due to the fast-changing intensity

near the edge of the Gaussian-shaped laser beams used in the interference lithography, the nanostructure geometry has a much larger gradient near the sensor edge. R = 8 and 9 mm positions are close to the edge and the nanostructures within the 0.09 $mm^2$ sampling region have noticeable dimensional change. Therefore, the experimental spectrum at the R = 9 mm position is an average spectrum from holes with different diameters, and shows deviation from the simulation results obtained on uniform nanostructures with dimensions determined from SEM pictures. In addition, note that a feature corresponding to Wood's anomaly occurs at a constant wavelength of ~ 790 nm for all the structures, which is also observed in the measured spectra.

The top-view and cross-section electric field distributions around a nanopillar, a nanosquare, and a nanohole, which correspond to the positions at R = 5 mm, R = 7 mm, and R = 9 mm, are also obtained through numerical modeling, are shown in Figure 3c. The electrical field enhancement at the various nanostructures at the 850 nm illumination wavelength is determined not only by the intrinsic resonance strength but also by the differences between the resonance wavelength and the illumination wavelength. For the nanopillar at the R = 5 mm position, resonance occurs around the illumination wavelength; thus, a large electric field enhancement occurs. The enhanced electric fields are tightly confined to the surrounding outer volume of the nanostructures and overlap with the captured molecular thin layers, which is ideal for sensing applications.

To evaluate the near-field sensing capability of the gradient plasmonic metasurface sensing chip, we acquired the transmission intensity pattern on the metasurface with various covering $Al_2O_3$ molecules. $Al_2O_3$ of various thicknesses is deposited by atomic layer deposition (ALD) in 10 consecutive runs, and each run deposits 12 layers of $Al_2O_3$ molecules, amounting to 1.068 nm. Eleven transmission images of the same sensor chip with $Al_2O_3$ thicknesses from 0 to 10 × 1.068

nm are recorded, and the collection is shown in **Figure 4**b. The intensity distributions are extracted with an image processing algorithm by calculating the intensity from the pattern center to the edge along the radial direction, with the averaging of all pixels of equal radius. As displayed in Figure 4a, with increasing $Al_2O_3$ thickness, a center shift of the intensity-position dip is observed, which corresponds to a center shift of the dark ring in the image labelled with a red dashed line (Figure 4b). The dip position shift versus the thickness of $Al_2O_3$ is plotted and linearly fitted in Figure 4c, and the error bars are the standard deviation calculated from three repeated experiments. Detection sensitivity of 12.78 pixels/12 layers of $Al_2O_3$ molecules with good linear dependence is obtained, indicating that even one layer of $Al_2O_3$ molecules can be observed and leads to a more than one pixel shift in our sensing platform. It should be noted that, the nearly linear relation between the dip shift and the thickness is only maintained up to 25 nm thick deposited layer according to our numerical simulation. Beyond this, the dip shift will saturate due to the limited penetration of the near-field electrical field near the surface of the plasmonic metasurface.

We applied this imaging-based gradient plasmonic metasurface sensing chip in a microfluidic detection setup to quantitatively analyze the BSA/anti-BSA immune complex formation. A fluidic device that combines the metasurface sensing chip with a PDMS chamber is fabricated (Figure S6, Supporting Information). The sensing microfluidic device is first initialized by flowing phosphate-buffered saline (PBS) buffer solution. Then, 1 mg $mL^{-1}$ BSA in PBS solution is injected into the chamber. Once a stable state is reached after half an hour, the dip shift of 11 pixels in the transmission pattern reveals the saturated adsorption of BSA molecules on the sensing chip surface. After that, anti-BSA solutions with various concentrations ranging from 0.2 to 10 μg $mL^{-1}$ are injected into the microchamber, and the treatment time in each test is more than 30 min to allow sufficient reaction with BSA proteins. After each measurement, the chamber and tubes filled with the low concentration anti-BSA solution are drained and then flushed with PBS solution for 20 min before filled with the anti-BSA solution with a higher

concentration. Figure 4d presents the radial distribution of the transmission intensity recorded on the metasurface. The specific binding of BSA and anti-BSA proteins on the gold metasurface leads to the shift of the transmission intensity dip due to the local refractive index change near the metasurface. As shown in Figure 4e, the binding of anti-BSA proteins at concentrations of 0.2, 0.5, 1, 2, 5, and 10 μg $mL^{-1}$ causes the transmission intensity dip to shift by 1, 2, 3, 4, 5, and 6 pixels, respectively, corresponding to 6.9, 13.8, 20.7, 27.6, 34.5, and 41.4 μm changes in the radius of the dark ring observed on the gold metasurface. The kinetic responses with varying concentrations of anti-BSA solutions was recorded with the injection of the anti-BSA solutions, as shown in Figure S6 in the Supporting Information.The dip positions become stable over time, which proves the affinity interaction between BSA and anti-BSA proteins.

The reversibility of the BSA/anti-BSA binding reaction suggests that the Langmuir isotherm model can be used for the quantitative assessment[15] of our sensor. Assuming a linear relationship between the shift of the transmission intensity dip and the fractional occupancy of the adsorption sites by the analyte molecules, the Langmuir isotherm model can be expressed as:

$$\Delta x = \Delta x_{sat} \frac{Kc}{1 + Kc}$$

where $\Delta x_{sat}$ is the saturation value of pixel shift $\Delta x$, $K$ is the associated equilibrium constant, and $c$ is the concentration of the anti-BSA solution. Fitting the measured intensity dip shift and the solution concentration, as shown in Figure 4e, we can obtain the fitted value for the equilibrium constant $K$ to be $0.69 \times 10^8$ $M^{-1}$, a value well in line with data from the reported literature.[16]

The sensitivity of the imaging-based sensing scheme is evaluated using the shift of the minima in the intensity pattern induced by the unit change of the refractive index of the medium covering the sensor. As depicted in **Figure 5**a, the intensity as a function of the radial distance from the center is determined by averaging the intensity values of a few thousand pixels on a narrow ring, which contributes to a highly enhanced signal-to-noise ratio by suppressing noises from recording and fabrication defects. A series of refractive index liquids (refractive index n from 1.30 to 1.38) is used as the covering medium to record corresponding transmission images, from which Figure 5b is obtained. The red arrow in Figure 5b indicates that the transmission dip moves towards the sensor center when the covering medium has a higher refractive index. By fitting the position of the transmission dips, the sensitivity $S_m$ is estimated to be 1040 pixel RIU$^{-1}$. The limit of detection (LOD) is calculated as $A/S_m$, where $S_m$ is the sensitivity and $A$ is the resolution of this method, which is taken as 1 pixel before applying further data processing algorithms. The LOD of this new sensing scheme is therefore determined to be 0.00096 RIU. Furthermore, according to the experimental data on the sensitivity and the spatial range of dip shift, we estimate that our sensor can work under background refractive index as high as 1.7, which could cover most detection scenario.

Further improvement of the sensitivity of our imaging-based metasurface sensors is possible. $S_m$ can be derived using the following equation:

$$S_m = \frac{S \cdot D}{d\lambda_r(R)/\, dR}$$

where $S$ is the spectral sensitivity, i.e., the spectral shift in the transmission spectrum corresponding to unit refractive index change, of the metasurface building blocks. $D$ is the number of imaging pixels per unit length on the metasurface. $R$ is the radial distance. $\lambda_r(R)$ is the resonance wavelength in the transmission spectrum of the nanostructure at the position with a radial distance $R$. The sensitivity of the imaging-based sensing scheme, $S_m$, can be improved

by using a nanostructure design with higher spectral sensitivity $S$. $S_m$ can also be enhanced with slow change of the nanostructure geometry, i.e., smaller gradient, to contribute a smaller $d\lambda_r(R)/dR$ (Figure S7, Supporting Information). In addition to the metasurface design, optimization of the imaging design by using a zoom lens and an imager with more pixels will further enhance the sensitivity by increasing the parameter $D$. Ultimately, the fabrication quality of the metasurface sensor, such as the local geometry variation of the metasurface structures and the defect density, will largely account for the experimental sensitivity. Moreover, further improved image processing algorithms, such as using curve fitting across a larger or the whole set of pixels to detect the intensity image change with the adsorbed molecules, instead of tracing the single pixel at the minimum intensity dip, can potentially enhance the sensitivity of the proposed sensors.

On the Au nanodisk structures located 2 mm from the center of our metasurface sensor, we measured a spectral sensitivity of 261.5 nm $RIU^{-1}$ (Figure 5e, f) by monitoring the spectral shift using a typical laboratory spectrometer (e.g., QE65 Pro from Ocean Optics as used in this work), corresponding to a spectrometer-based LOD of 0.00076 ~ 0.00305 RIU at a spectral resolution ranging from 0.2 to 0.8 nm. Therefore, our imaging-based sensor has a LOD comparable to that of the spectrometer-based method while being more cost-effective and compact. The imaging-based method also features a high signal-to-noise ratio which benefits from a large number of pixels in a ring used in obtaining the average intensity (Figure S9, Supporting Information). Specifically, there are approximately 4000 pixels at the ring corresponding to the concerned dip in the intensity-position curve, while on the spectrometer only 50 pixels are averaged for each spectral data. The imaging-based sensing scheme uses a LED source without collimating optics, and the overall device can be compact and lightweight and suitable for point-of-care biosensing applications.

In conclusion, we have demonstrated an ultrasensitive sensor that can detect an angstrom-thick layer of adsorbed molecules through image acquisition and processing. Our imaging-based sensor has a LOD comparable to that of the spectrometer-based method while being more cost-effective and compact. The sensitivity can be further enhanced by exploring alternative materials, resonant nanostructures, and pattern designs. This novel sensing scheme is expected to be a promising platform for point-of-care and lab-on-chip applications, where an off-the-shelf monochromatic light source coupled with a commercial image sensor and an image processing chip can build up the platform.

**Experimental Section**

*Metasurface Template Fabrication:* A Si template with a concentric gradient metasurface was patterned using non-uniform interference lithography followed by inductively coupled plasma (ICP) etching, chrome evaporation, and lift-off processes. First, a Si substrate was spin-coated with a 200 nm thick anti-reflection coating (ARC, AZ Barli II, MicroChemicals) and baked at 200 °C for 1 min. Then, 20 nm-thick $SiO_2$ was deposited at a rate of 2 Å $s^{-1}$ using electron-beam evaporation. Next, a thin adhesive layer (Ti Prime, MicroChemicals) and a 200 nm thick positive photoresist (AZ MiR 701, MicroChemicals) film were spin-coated. The adhesive layer was baked at 120 °C for 2 min, and the photoresist film was baked at 90 °C for 1 min. Thereafter, the photoresist was double exposed to 405 nm wavelength light using a homemade interference lithography setup. The expansion distances of the two laser beams were only 25 cm, far less than that in conventional interference lithography, leading to a non-uniform intensity profile. The angle between the two beams was 43.2° for the 550 nm pattern period. The highest exposure intensity was 430 μW $cm^{-2}$, which occurred at the pattern center. The two exposures were orthogonal, and each lasted for 42 s. The photoresist was then immersed in a 1:4 diluted developer (AZ 351B, Clariant) for 1 min. After patterning the photoresist, the $SiO_2$ and ARC

layers were etched using $CHF_3$ and $O_2$ plasma in an ICP system, respectively. To transfer the metasurface pattern into Si, a 50 nm-thick chrome hard mask was deposited using electron-beam evaporation, and lift-off was performed with ultrasonic agitation in RCA-1 solution ($NH_3 \cdot H_2O:H_2O_2:H_2O$ = 1:1:5) at 75 °C for 3 min. The mask pattern was transferred into Si with a 200 nm structure depth by $CHF_3/SF_6$ plasma in the ICP system with 53/10 sccm flow rates, a 5 mTorr pressure, a 150 W source power, and a 50 W bias power. Finally, the Cr mask was dissolved to complete the Si metasurface template fabrication (Figure S2, Supporting Information).

*Gold Metasurface Fabrication:* The metasurface pattern was replicated by thermal nanoimprint lithography using a nanoimprinting platform consisting of electrically heated platens with a temperature controller (Specac Ltd.), a hydraulic press (Specac Ltd.), and a chiller (Grant Instruments). A UV-cured molding material (OrmoStamp, micro resist technology GmbH) was applied to fabricate the thermal nanoimprint mold. The Si template pattern was transferred through UV-nanoimprint lithography and then modified with a hydrophobic self-assembled monolayer (FDTS, RHAWN). To prepare the gold metasurface, a cleaned glass substrate was first spin-coated with Ti Prime (MicroChemicals) as an adhesive layer, followed by the deposition of ARC, $SiO_2$, and Ti Prime layers following the same process as the Si template fabrication flowchart. Afterward, 95 nm poly(n-butyl methacrylate)-based thermal nanoimprint resist (Dongguan Jincai Materials) was spin-coated and baked at 100 °C for 20 min. The resist was imprinted using the OrmoStamp mold under a pressure of 4.4 MPa at 100 °C for 15 min, and this pressure was maintained until the temperature decreased below 45 °C. The residual resist layer was removed by $O_2$ plasma in the ICP system. Similar to the Si template fabrication process, the $SiO_2$ and ARC were further etched. Then, 3 nm Cr and 50 nm Au were deposited at rates of 0.3 Å $s^{-1}$ and 0.5 Å $s^{-1}$, respectively, using electron-beam evaporation. The gold metasurface was finally obtained after performing lift-off in RCA-1 solution to remove the metal on top of the ARC (Figure S2, Supporting Information).

*Image-based Sensing Setup and Data Processing:* Transmission images of the gradient metasurface were captured using a commercial monochromatic CMOS image sensor equipped with a cooling system (QHY183M). A lens (Micro-Nikkor 55 mm F/2.8, Nikon) was applied in the optical path. The exposure time of each image, which was composed of 5544 × 3694 effective pixels in 16 bit, was 5 ms (gain = 30). A monochromatic uniform light source was generated by an LED panel (134 × 76 × 2.5 $mm^3$) together with a narrowband optical filter (diameter = 40 mm) with an 850 nm central wavelength and an 11 nm FWHM. Intensity-position curves were extracted from transmission images by an algorithm. Specifically, each point in the curve was calculated by averaging all pixels of equal radius, and then, curve smoothing was applied to reduce the effect of sample defects.

*Refractometric Sensitivity Measurements:* Refractive index standard liquids (Cargille Labs) were dropped on the sample, and a cleaned cover glass (2.4 cm × 2.4 cm × 0.17 mm) was applied on the sample surface to help the liquid spread. The standard liquids had refractive indices of 1.30, 1.31, 1.32, 1.34, and 1.38. After each recording of the transmission image, the sample was thoroughly rinsed with acetone and isopropanol before being dried under nitrogen flow.

*$Al_2O_3$ Molecular Layers Deposition:* $Al_2O_3$ molecular layers were deposited on the sensing chip by ALD in a Savannah S200 ALD chamber (Ultratech). To prevent the deformation of the gold metasurface, the temperatures of both the reactor line heater and chamber heater were maintained at 80 °C. The TMA precursor was kept at room temperature. One deposition cycle included a 0.015 s pulse of TMA and a 0.015 s pulse of water, and the waiting times after the pulses were 30 s and 60 s, respectively. The pressure during the deposition was 0.67 Torr.

*Biosensing Performance Measurement:* The gold metasurface sensing chip was integrated with a polydimethylsiloxane (PDMS) chamber (inner volume: 2.2 cm × 2.2 cm × 1.1 mm) to assemble a simple microfluidic device for biosensor experiments. A liquid was injected through

a tube by an injection pump (LongerPump) and flowed out from another tube (Figure S6a, Supporting Information). The sensing microfluidic device was first initialized by flowing PBS buffer solution (BBI Life Sciences). Then, BSA (Solarbio) in PBS solution at a 1 mg $mL^{-1}$ concentration was injected. Half an hour later, the anti-BSA solutions (Proteintech) were injected into the microchamber at various concentrations ranging from 0 to 10 μg $mL^{-1}$ in PBS buffer solution and allowed to stand for more than 30 min. After each measurement, the chamber and tubes filled with the low concentration anti-BSA solution were drained, and then, the microfluidic device was flushed with PBS solution for 20 min. Finally, it was drained again to prepare for the next higher concentration test.

*Measurement of Transmission Spectra:* VIS-NIR spectra were collected using a spectrometer (QE65Pro, Ocean Optics) with a 0.74 nm data interval. The sample was illuminated by a normal incidence unpolarized broadband light source (LG-PS2, Olympus), and the transmission spectra in a 0.09 $mm^2$ region confined by an optical aperture were obtained. A manual displacement stage with a resolution of 0.01 mm was applied to sweep the transmission spectra of the sample at positions of R = 0 mm, 2 mm, 4 mm, 5 mm, 6 mm, 7 mm, 8 mm, and 9 mm. All presented spectra were normalized by dividing them by the transmission spectra of a glass substrate and underwent ten times averaging together with curve smoothing.

*Morphological Characterizations:* SEM (Merlin, Zeiss) was used to characterize the morphology of the samples. Firstly, we took the SEM images across the whole metasurface to obtain 10 × 10 SEM images with the spatial coordinates recorded through an automatic script. Then, *ProSEM* software was applied to extract the geometric parameters, such as the pillar/hole diameters, from the SEM images. The optical characterization was done on the same positions where the SEM pictures were taken to link the microscopic morphology of the plasmonic structures with their optical behaviors.

*FDTD Simulations:* Numerical analysis of the transmission spectra and electric field distribution was performed using the commercially available software FDTD Solutions (Lumerical Solutions Inc.). The geometric parameters at each position were determined from the corresponding SEM images, and the simulation results were produced by treating the localized nanostructures as uniform using periodic boundary conditions along the x- and y-axes. Perfect matching layers (PML) were applied to eliminate any reflection in the top and the bottom boundaries. A non-uniform mesh with a maximum mesh step of 1 nm was applied. All the nanostructures were drawn with rounded edges and corners of a 5 nm radius. The material parameters used for chrome and gold in the VIS-NIR region were from the CRC model.

**Supporting Information**

Supporting Information is available from the Wiley Online Library or from the author.

**Acknowledgements**

This work was partially supported by the General Research Fund of the Research Grants Council of the Hong Kong Special Administrative Region (Awards No. 17207419 and 17209320), the Platform Technology Funding program and the Seed Funding Programme for Basic Research (201811159244) of the University of Hong Kong. The authors acknowledge the technical support from SUSTech CRF. We would also like to thank Yanling He for assistance in $Al_2O_3$ deposition, and Shuangwen Chen, from Carl Zeiss (Shanghai) Co., Ltd, for the collection of SEM images.

References

[1] L. Huang, X. Chen, H. Mühlenbernd, H. Zhang, S. Chen, B. Bai, Q. Tan, G. Jin, K.-W. Cheah, C.-W. Qiu, J. Li, T. Zentgraf, S. Zhang, *Nat. Commun.* **2013**, 4, 2808; N. Meinzer, W. L. Barnes, I. R. Hooper, *Nat. Photonics* **2014**, 8, 889; A. Shaltout, J. Liu, A. Kildishev, V. Shalaev, *Optica* **2015**, 2, 860.

[2] A. M. Shaltout, K. G. Lagoudakis, J. van de Groep, S. J. Kim, J. Vučković, V. M. Shalaev, M. L. Brongersma, *Science* **2019**, 365, 374; R. C. Devlin, M. Khorasaninejad, W. T. Chen, J. Oh, F. Capasso, *Proc. Natl. Acad. Sci. USA* **2016**, 113, 10473; R. J. Lin, V. C. Su,

S. Wang, M. K. Chen, T. L. Chung, Y. H. Chen, H. Y. Kuo, J. W. Chen, J. Chen, Y. T. Huang, J. H. Wang, C. H. Chu, P. C. Wu, T. Li, Z. Wang, S. Zhu, D. P. Tsai, *Nat. Nanotechnol.* **2019**, 14, 227.

[3] F. Capasso, *Nanophotonics* **2018**, 7, 953; S. Chen, W. Liu, Z. Li, H. Cheng, J. Tian, *Adv. Mater.* **2020**, 32, 1805912; P. Genevet, F. Capasso, F. Aieta, M. Khorasaninejad, R. Devlin, *Optica* **2017**, 4, 139; H.-H. Hsiao, C. H. Chu, D. P. Tsai, *Small Methods* **2017**, 1, 1600064; V. C. Su, C. H. Chu, G. Sun, D. P. Tsai, *Opt. Express* **2018**, 26, 13148; W. Liu, D. Ma, Z. Li, H. Cheng, D. Y. Choi, J. Tian, S. Chen, *Optica* **2020**, 7, 1706.

[4] B. García-Cámara, R. Gómez-Medina, J. J. Sáenz, B. Sepúlveda, *Opt. Express* **2013**, 21, 23007; Y. Lee, S. J. Kim, H. Park, B. Lee, *Sensors* **2017**, 17, 1726; A. Tittl, H. Giessen, N. Liu, *Nanophotonics* **2014**, 3, 157; Y. Yang, Kravchenko, II, D. P. Briggs, J. Valentine, *Nat. Commun.* **2014**, 5, 5753; G. Zhang, C. Lan, H. Bian, R. Gao, J. Zhou, *Opt. Express* **2017**, 25, 22038; Y. Zhang, W. Liu, Z. Li, Z. Li, H. Cheng, S. Chen, J. Tian, *Opt. Lett.* **2018**, 43, 1842.

[5] Y. Chang, D. Hasan, B. Dong, J. Wei, Y. Ma, G. Zhou, K. W. Ang, C. Lee, *ACS Appl. Mater. Interfaces* **2018**, 10, 38272; N. A. Joy, M. I. Nandasiri, P. H. Rogers, W. Jiang, T. Varga, S. V. Kuchibhatla, S. Thevuthasan, M. A. Carpenter, *Anal. Chem.* **2012**, 84, 5025; A. W. Powell, D. M. Coles, R. A. Taylor, A. A. R. Watt, H. E. Assender, J. M. Smith, *Adv. Opt. Mater.* **2016**, 4, 634.

[6] P. H. Rogers, G. Sirinakis, M. A. Carpenter, *J. Phys. Chem. C* **2008**, 112, 8784; L. Wang, Y. Zhu, L. Xu, W. Chen, H. Kuang, L. Liu, A. Agarwal, C. Xu, N. A. Kotov, *Angew. Chem. Int. Ed.* **2010**, 49, 5472.

[7] H. Im, H. Shao, Y. I. Park, V. M. Peterson, C. M. Castro, R. Weissleder, H. Lee, *Nat. Biotechnol.* **2014**, 32, 490; S.-W. Lee, K.-S. Lee, J. Ahn, J.-J. Lee, M.-G. Kim, Y.-B. Shin, *ACS Nano* **2011**, 5, 897.

[8] M. Riskin, R. Tel-Vered, O. Lioubashevski, I. Willner, *J. Am. Chem. Soc.* **2009**, 131, 7368; C. Situ, M. H. Mooney, C. T. Elliott, J. Buijs, *Trends Analyt. Chem.* **2010**, 29, 1305.

[9] I. H. El-Sayed, X. Huang, M. A. El-Sayed, *Nano Lett.* **2005**, 5, 829; B. S, B. S, G. S, *J. Nanomed. Nanotechnol.* **2016**, 7, 1000373.

[10] J. Bian, X. Xing, S. Zhou, Z. Man, Z. Lu, W. Zhang, *Nanoscale* **2019**, 11, 12471.

[11] A. Tittl, A. John-Herpin, A. Leitis, E. R. Arvelo, H. Altug, *Angew. Chem. Int. Ed. Engl.* **2019**, 58, 14810.

[12] F. Yesilkoy, E. R. Arvelo, Y. Jahani, M. Liu, A. Tittl, V. Cevher, Y. Kivshar, H. Altug, *Nat. Photonics* **2019**, 13, 390.

[13] C. Liang, T. Qu, J. Cai, Z. Zhu, S. Li, W. D. Li, *Opt. Express* **2018**, 26, 8194; Z. Gan, J. Cai, C. Liang, L. Chen, S. Min, X. Cheng, D. Cui, W.-D. Li, *J. Vac. Sci. Technol. B* **2019**, 37, 060601.

[14] C. Zhang, H. Subbaraman, Q. Li, Z. Pan, J. G. Ok, T. Ling, C.-J. Chung, X. Zhang, X. Lin, R. T. Chen, L. J. Guo, *J. Mater. Chem. C* **2016**, 4, 5133.

[15] C. Kotlowski, P. Aspermair, H. U. Khan, C. Reiner-Rozman, J. Breu, S. Szunerits, J.-J. Kim, Z. Bao, C. Kleber, P. Pelosi, W. Knoll, *Flex. Print. Electron.* **2018**, 3, 034003.

[16] W. C. Olson, T. M. Spitznagel, M. L. Yarmush, *Mol. Immunol.* **1989**, 26, 129.

**Figure 1**

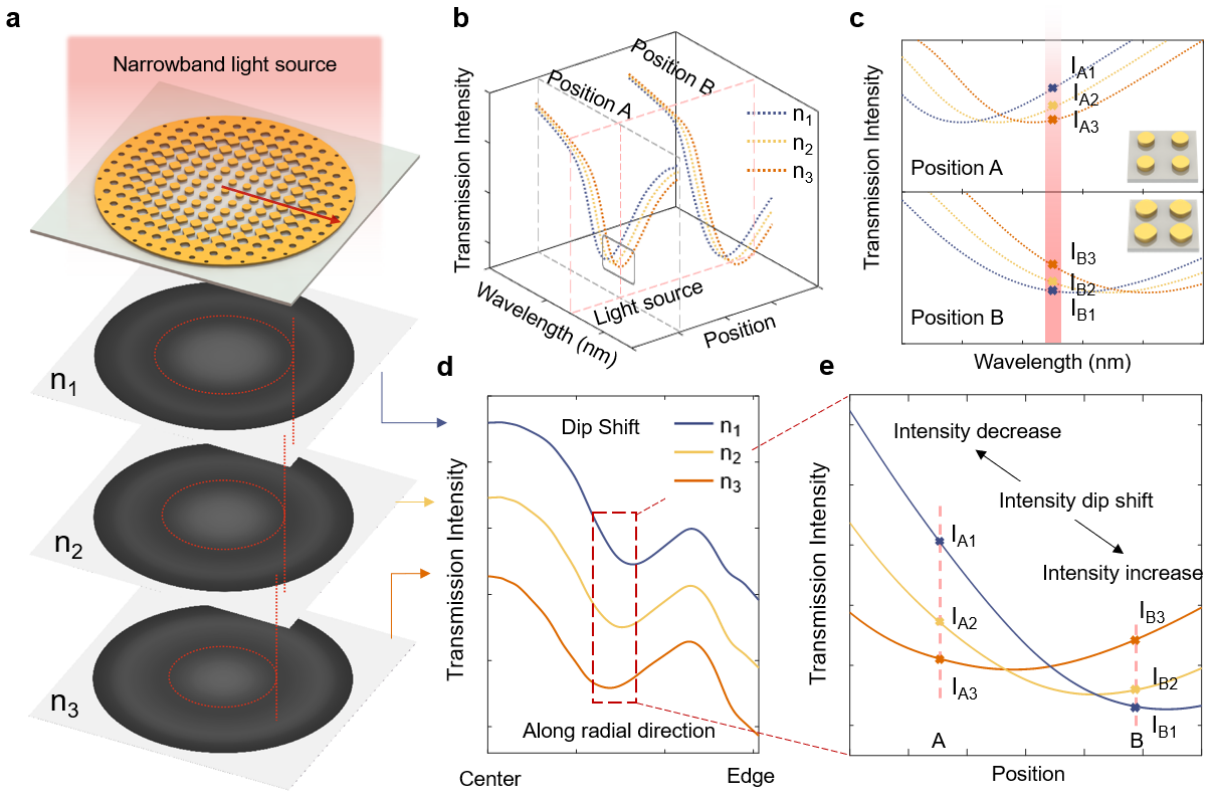


**Figure 1.** Scheme of the space-multiplexed imaging-based molecular detection on a circular gradient plasmonic metasurface. (a) The sensing chip illuminated by a narrowband light source exhibiting different transmission intensity patterns with different background refractive indices. (b) Schematic plot of transmission spectra at two positions under background refractive indices of $n_1$, $n_2$, and $n_3$. (c) Zoomed-in spectra of (b) with the wavelength of the narrowband light source marked. (d) Transmission intensity distribution extracted from (a). The shift of the dip in the intensity curves corresponds to a decrease in the dark ring radius. (e) Zoomed-in transmission intensity of (d). The intensity value at a specific position can be extracted from the corresponding spectra.

**Figure 2**

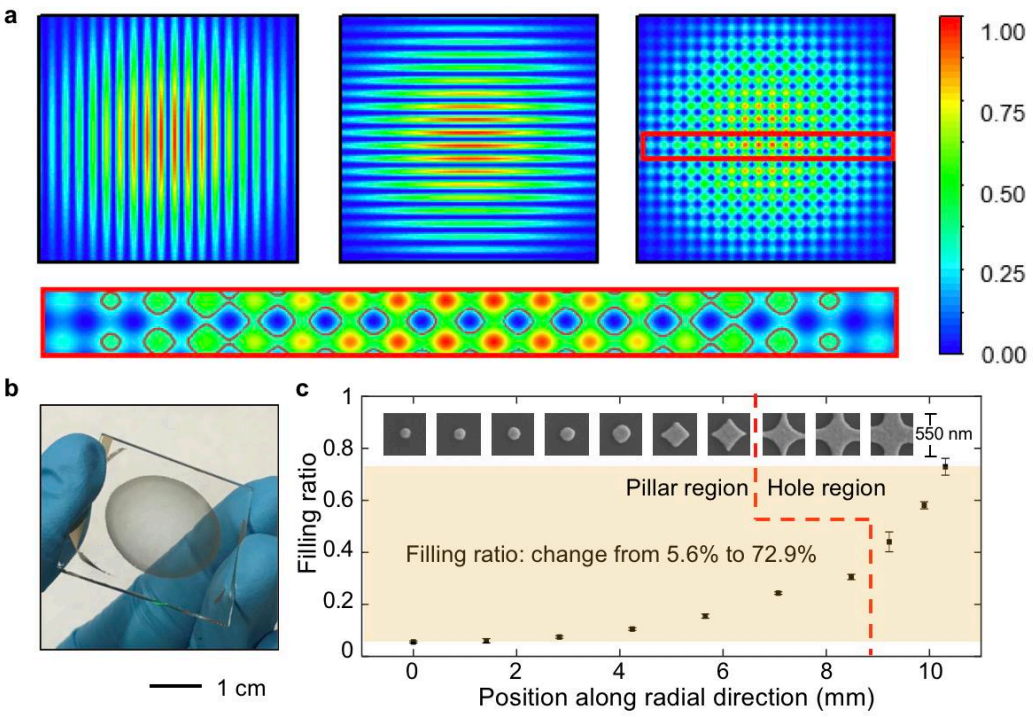


**Figure 2.** Deterministic fabrication of gradient nanostructures using non-uniform Gaussian-shaped coherent beams in interference lithography. (a) The schematic diagram of intensity distributions of the interference pattern from two coherent laser beams with non-uniform Gaussian-shaped intensity profile. (b) Photograph of a sensing chip consisting of a gold metasurface with concentric gradient nanostructures. (c) Plot of the filling ratio versus position along the radial direction. The insets are SEM images of unit structures at corresponding positions.

**Figure 3**

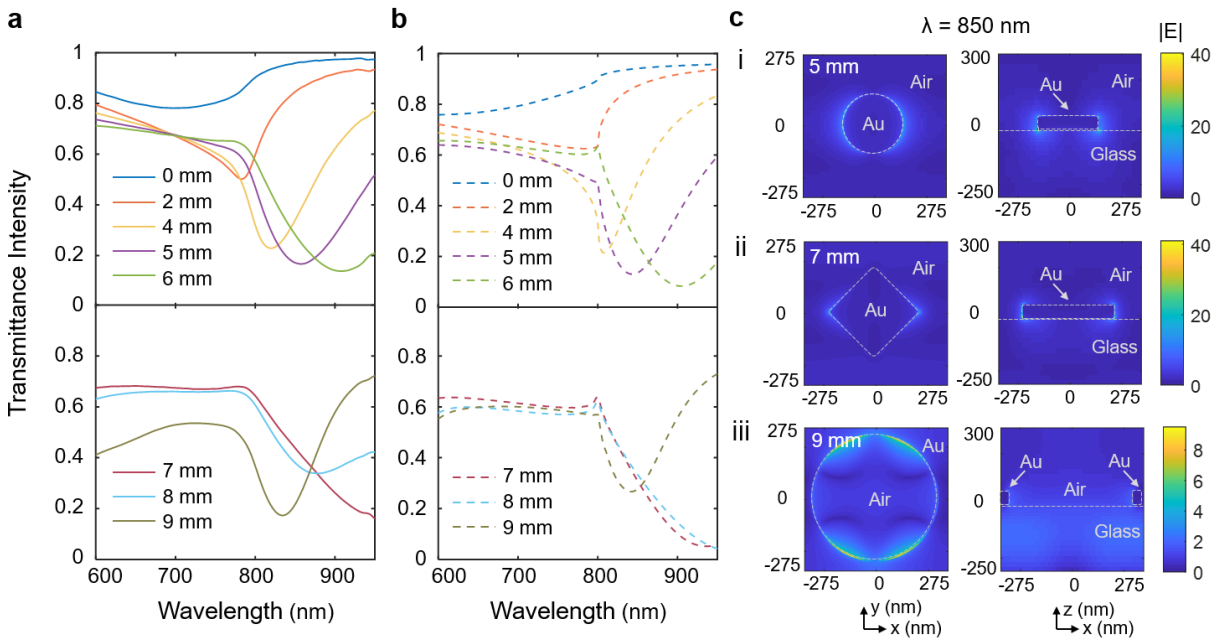


**Figure 3.** Measurement and modeling of the optical properties of the gradient metasurface. (a) Measured transmission spectra along the radial direction. (b) Simulated transmission spectra at corresponding positions. (c) Top-view electrical distribution of a nanopillar, a nanosquare, and a nanohole at an 850 nm illumination wavelength.

**Figure 4**

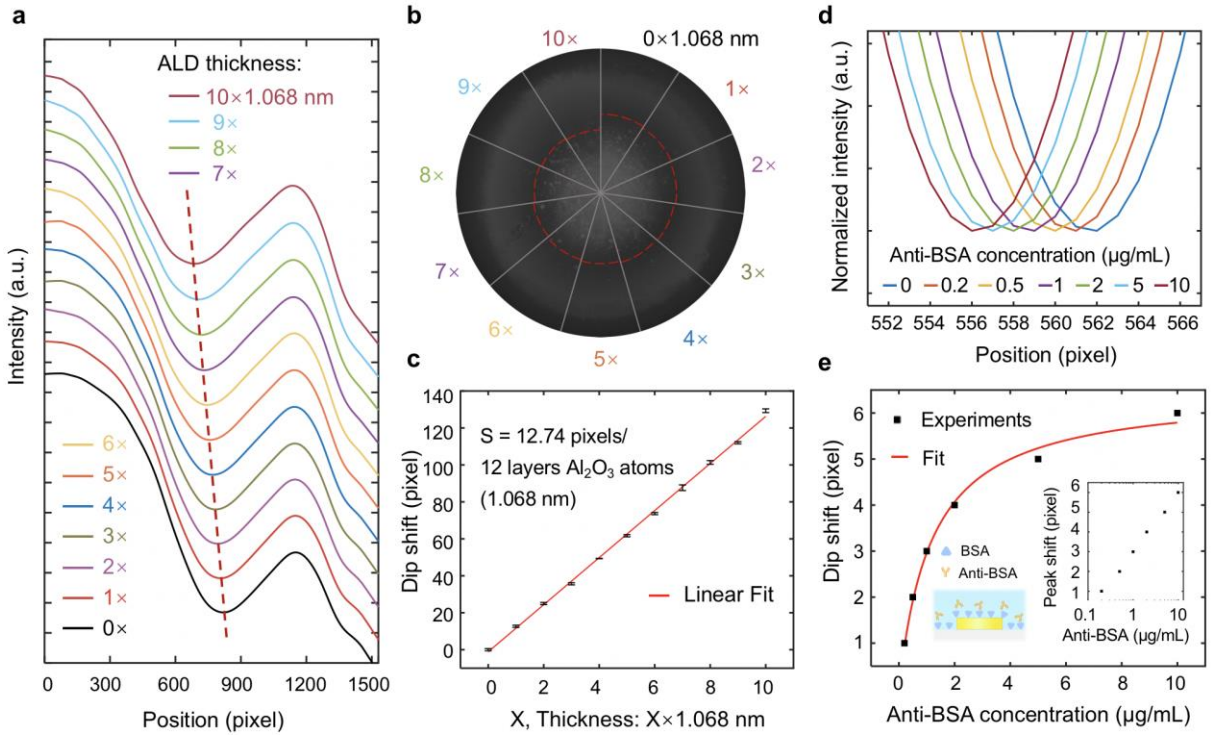


**Figure 4.** Demonstration of the detection of various molecules attached on the metasurface. (a) Intensity distributions extracted from transmission images when $Al_2O_3$ of various thicknesses is deposited by ALD in 10 consecutive runs, and each run deposits 1.068 nm of $Al_2O_3$. (b) Collection of transmission images after each $Al_2O_3$ deposition run. (c) Plot of the intensity dip (labeled in (a) by the red dashed line) shift versus $Al_2O_3$ thickness; the error bars indicate standard deviations from three measurements. With linear fitting, one layer of $Al_2O_3$ leads to approximately one pixel shift. (d) Spatial distribution of transmission intensity obtained on the gradient metasurface after being treated with anti-BSA solutions of various concentrations. (e) Measured intensity dip position shifts as a function of anti-BSA concentration. The orange line is a Langmuir function fit to the anti-BSA concentrations from 0.2 to 10 μg $mL^{-1}$. The inset shows the shift in a log-linear graph.

**Figure 5**

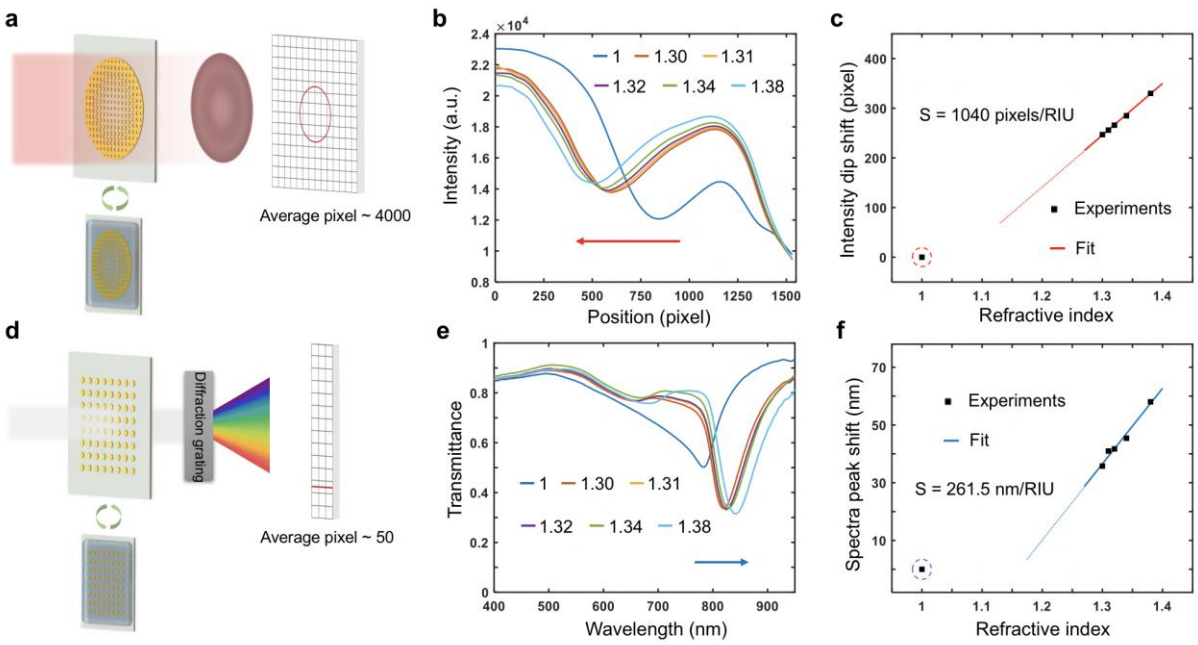


**Figure 5.** Analysis of the detection limit of the imaging-based sensing scheme. (a) Schematic of the imaging-based gold metasurface sensing platform. The transmission intensity as a function of radial distance is determined by averaging pixels in a narrow ring region, as represented by the red circle. (b) Transmission intensity distribution measured on the metasurface sensor covered with air (n = 1.0) and different standard refractive index liquids (n = 1.30 ~ 1.38). (c) Plot of the linear fitting of the intensity dip shift and the medium refractive index. (d) Schematic of conventional spectrometer-based sensing scheme using dispersive elements and imaging sensors. The red line represents pixels on a imaging sensor that are averaged to obtain the spectral information. (e) Transmission spectra measured at R = 2 mm on the metasurface covered with different standard refractive index liquids (1.30 - 1.38). (f) Plot of the linear fitting of the resonant wavelength shift versus the medium refractive index. Note that the n = 1.0 point (dashed circle) is excluded from the fitting in (c) and (f).

**TOC**

An ultrasensitive sensor that can detect an angstrom-thick layer of adsorbed molecules by imaging of centimeter-scale plasmonic metasurface is demonstrated. This novel sensing scheme is expected to be a promising platform for point-of-care and lab-on-chip applications, which can be realized using off-the-shelf monochromatic light sources and commercial image sensors.

**Keywords**

molecular detection, image-based sensing scheme, centimeter-scale metasurfaces, deterministic gradient geometry

**Authors**

S. Min, S. Li, Z. Zhu, Y. Liu, C. Liang, J. Cai, F. Han, Y. Li, W. Cai, X. Cheng*, and W.-D. Li*

**Title**

**Ultrasensitive Molecular Detection by Imaging of Centimeter-scale Metasurfaces with a Deterministic Gradient Geometry**